Eur Biophys J (2009) 39:149–165
DOI 10.1007/s00249-009-0469-2

ORIGINAL PAPER

Effectors of the frequency of calcium oscillations in HEK-293 cells: wavelet analysis and a computer model

David Szekely · Sarah C. Brennan · Hee-Chang Mun · Arthur D. Conigrave · Philip W. Kuchel

Received: 26 February 2009 / Revised: 22 April 2009 / Accepted: 29 April 2009 / Published online: 3 June 2009

Abstract Oscillations of the intracellular concentration of Ca^{2+} in cultured HEK-293 cells, which heterologously expressed the calcium-sensing receptor, were recorded with the fluorophore Fura-2 using fluorescence microscopy. HEK-293 cells are extremely sensitive to small perturbations in extracellular calcium concentrations. Resting cells were attached to cover slips and perifused with saline solution containing physiologically relevant extracellular Ca^{2+} concentrations in the range 0.5–5 mM. Acquired digitized images of the cells showed oscillatory fluctuations in the intracellular Ca^{2+} concentration over the time course, and were processed as a function of the change in Fura-2 excitation ratio and frequency at 12–37°C. Newly developed data processing techniques with wavelet analysis were used to estimate the frequency at which the rectified sinusoidal oscillations occurred; we estimated $\sim 4\ min^{-1}$ under normal conditions. Temperature variations revealed an Arrhenius relationship in oscillation frequency. A critical Ca^{2+} concentration of ~ 2 mM was estimated, below which oscillations did not occur. These data were used to develop a kinetic model of the system that was simulated using *Mathematica*; kinetic parameter values were adjusted to match the experimentally observed oscillations of intracellular Ca^{2+} concentration as a function of extracellular Ca^{2+} concentration, and temperature; and from these, limit cycles were obtained and control coefficients were estimated for all parameters.

Keywords Analytical kinetic model · Calcium-induced oscillations · Calcium-sensing receptor · Control coefficient · Fourier analysis · Fura-2 fluorescence microscopy · Limit cycle · Metabolic control analysis · Wavelet analysis

Abbreviations

1D	One-dimensional
2D	Two-dimensional
ATP	Adenosine triphosphate
CaR	Calcium sensing receptor
C_p^f	Control coefficient, frequency with respect to parameter value
DOG	Derivative of a Gaussian
EGTA	Ethylene glycol tetra acetic acid
ER	Endoplasmic reticulum
GTP	Guanosine triphosphate
HEK-293	Human embryonic kidney cells, Graham's experiment number 293
IP_3	Inositol trisphosphate
IP_3R	IP_3 receptor
K_d	Dissociation constant
K_M	Michaelis constant
PKC	Protein kinase C
PMCA	Plasma membrane Ca^{2+}-ATPase
SERCA	Sarcoplasmic/endoplasmic reticulum Ca^{2+}-ATPase
t	Time

"Proteins, membranes and cells: the structure-function nexus." Contributions from the annual scientific meeting (including a special symposium in honour of Professor Alex Hope of Flinders University, South Australia) of the Australian Society for Biophysics held in Canberra, ACT, Australia, 28 September–1 October 2008.

D. Szekely · S. C. Brennan · H.-C. Mun · A. D. Conigrave · P. W. Kuchel (✉)
School of Molecular and Microbial Biosciences, University of Sydney, Building G08, Sydney, NSW 2006, Australia
e-mail: p.kuchel@mmb.usyd.edu.au

P. W. Kuchel
Centre for Mathematical Biology, University of Sydney, Sydney, NSW 2006, Australia

Introduction

There has been much recent interest in the oscillations in cellular Ca^{2+} concentrations in various cell types brought about through interactions with extracellular Ca^{2+} (Marhl et al. 2008; Breitwieser 2006; Sneyd et al. 2003). Cytoplasmic Ca^{2+} in human embryonic kidney (HEK)-293 cells exchanges with endoplasmic reticulum (ER) and mitochondrial stores, and undergoes regulated influx and efflux with the extracellular space (Breitwieser and Gama 2001). Excess Ca^{2+} is either transported out of the cell or pumped back into intracellular stores. Changes in cytoplasmic Ca^{2+} concentration constitute regulatory signals in cellular mechanisms that control the magnitude and frequency of variations in cytoplasmic Ca^{2+} concentration. In human plasma, the Ca^{2+} concentration is normally held in the range 1.1–1.3 mM, and the total intracellular Ca^{2+} concentration varies between 0.1 and 0.5 mM; however, the free intracellular Ca^{2+} concentration is much lower (Conigrave et al. 2004). In addition to replenishing intracellular Ca^{2+} via influx through transporters and/or ion channels, extracellular Ca^{2+} serves as a first messenger, stimulating the plasma-membrane-localized calcium-sensing receptor (CaR) (Breitwieser 2006). The CaR in HEK-293 cells responds to elevated extracellular Ca^{2+} concentration by inducing a signaling cascade that causes short-term dynamic increases in cytoplasmic Ca^{2+} as intracellular stores are depleted. The low affinity of the CaR for extracellular Ca^{2+} (apparent $K_d \approx 2.5$ mM) implies that it is adapted to sensing small variations in extracellular Ca^{2+} concentration (Mun et al. 2004). Interestingly, activation of the CaR by elevated Ca^{2+} induces time-dependent variations in Ca^{2+} concentration (Breitwieser 2006; Falcke 2004).

We aimed to determine the effect of different temperatures and extracellular Ca^{2+} concentrations on time-dependent cytoplasmic Ca^{2+} fluctuations with a view to establishing a model to aid in elucidating the molecular and organelle-dependent basis of Ca^{2+}-induced Ca^{2+} oscillations.

Fura-2 is a fluorophore that binds to free intracellular Ca^{2+} with a high affinity ($K_d \approx 0.2$ μM); it is excited at a wavelength of 380 nm for the unbound form, and 340 nm for the Ca^{2+}-bound form; and the excitation ratio of the emission intensities at these wavelengths is directly correlated with the concentration of intracellular Ca^{2+}. The use of the fluorescence ratio affords independence from factors such as fluorophore concentration, autofluorescence, microscope focus drift, and background light. This makes Fura-2 experimentally useful for the detection of changes in intracellular Ca^{2+} in CaR-expressing HEK-293 cells. A proposal for the pathways by which extracellular Ca^{2+} binding to the CaR mediates changes in cellular Fura-2 fluorescence is given in Fig. 1 (Breitwieser 2006; Skupin and Falcke 2007).

Wavelet analysis is a relatively new data processing method that exploits the Fourier transform (Torrence and Compo 1998). The discrete wavelet transform represents a one-dimensional (1D) time series as a two-dimensional (2D) image, where the frequency components of a time series can be localized to every temporal domain. Since the data obtained in the current study were not purely sinusoidal, several artifacts emerged upon Fourier transformation. The discrete wavelet transform is preferable to the direct Fourier transform since many of the known artifacts in signal analysis can be eliminated, and visualization of small variations in frequency over the entire temporal domain can be achieved without the need for multiple computations.

Using wavelet analysis we were able to estimate the frequency of ratiometric oscillations in Fura-2 using fluorescence microscopy. The pathways for CaR-induced

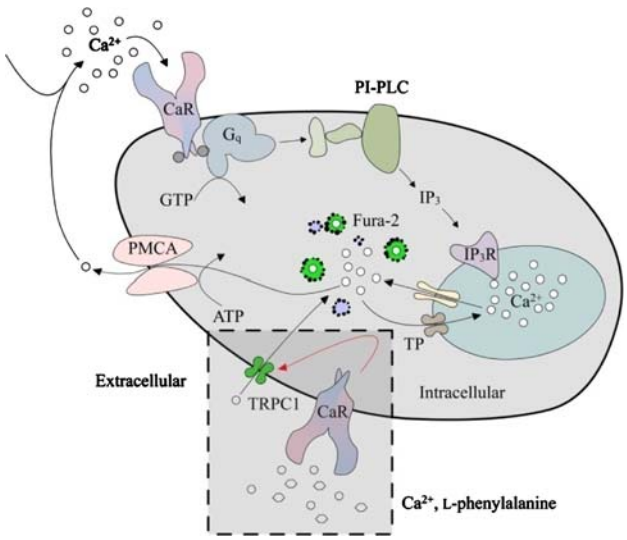

Fig. 1 Pathways for calcium-sensing receptor (CaR)-mediated induction of intracellular Ca^{2+} oscillations. Ca^{2+} activates the CaR, causing coupling to and activation of the heterotrimeric GTP binding protein Gq, which activates phospholipase C (PI-PLC), leading to production of inositol 1,4,5-trisphosphate (IP_3), which can activate IP_3 receptors (IP_3R) located on intracellular membranes, releasing stored Ca^{2+}. Increased intracellular Ca^{2+} is either pumped back into stores via a thapsigargin-sensitive pump (TP), or out of the cell via the plasma-membrane-localized Ca^{2+}-ATPase (PMCA). In restricted extracellular spaces, extracellular Ca^{2+} may increase as a result of PMCA activity, potentiating CaR activation. Ca^{2+}-induced oscillations are sinusoidal, on an elevated baseline of intracellular Ca^{2+} concentration. Oscillations may be the result of PKC-mediated phosphorylation of CaR and cyclical production of IP_3. The area enclosed by the dashed-outline grey box is a pathway for the influx of Ca^{2+} into the cytosol. The CaR senses L-phenylalanine, which induces the recruitment of transient receptor potential cation channel, subfamily C, member 1 (TRPC1) to the lipid bilayer, which allows influx of Ca^{2+} (Breitwieser 2006)

intracellular Ca^{2+} oscillations reported by Breitwieser (2006) were modeled, and parameter values were adjusted to give output that was consistent with our experimental findings. This model provided an experimental tool that is capable of predicting Ca^{2+} oscillatory features under diverse conditions, leading to a better understanding of the mechanisms of CaR operation and its effect on cytoplasmic Ca^{2+} concentration.

There has been recent interest in modeling the oscillations brought about by Ca^{2+}-induced Ca^{2+} release inside nonexcitable cells (Sneyd et al. 2003; Fioretti et al. 2005; Baker et al. 2002; Hofer 1999; Kusters et al. 2007). Predictions made by previous models included identifying factors that cause the oscillations (Fioretti et al. 2005; Baker et al. 2002). This type of modeling is less appealing since the primary oscillatory response is directly determined by the modeler driving the system with oscillations of an input solute, rather than allowing the oscillations to emerge from feedback and feedforward control processes. For example, to show that Ca^{2+} oscillations are caused by binary switching of the activity of CaR, the programmer could assign a time-dependent binary function on the rate constant describing the forward reaction of the CaR, upon sensing Ca^{2+}. This would lead to intracellular Ca^{2+} oscillations, provided that the other parts of the model accommodated this feature appropriately. While this type of model would show that Ca^{2+} oscillations were caused by the dynamics of the CaR, it is not necessarily an accurate representation of the real system.

A model needs to be built upon a reaction scheme that represents the current consensus on the pathways of interest. The predictions drawn from it should not rely on the design of the model, but rather the consequences of simulating it. To our knowledge, an accurate model representing the HEK-293 cell, and in particular the reaction scheme proposed by (Breitwieser 2006), does not exist. In the present work, we devised a system of first- and variable-order kinetic equations to describe this system. Model parameters were adapted from existing work or fitted to experimental data. In constructing this model, we aimed to make experimentally testable predictions which would lead to a greater understanding of the CaR system, which have not been achieved through other types of theoretical analyses and experiments.

Materials and methods

HEK-293 cell culture procedure

The methods used to derive the clone of HEK-293 cells that stably expressed the CaR are described in Mun et al. (2004); an outline of the methods, relevant to the present study, follow.

pcDNA3.1(+) (Invitrogen, Carlsbad, CA) containing the wild-type human CaR [cassette version, Bai et al. (1996)], was the gift of Dr. Mei Bai and Professor Edward Brown (Endocrine-Hypertension Division, Brigham and Women's Hospital, Boston, MA).

Transfection-grade DNA was prepared using the High-speed^{TM} midi kit (Qiagen, Valencia, CA). HEK-293 cells were cultured in Dulbecco's modified Eagle's medium (Invitrogen) containing 10% fetal bovine serum. When the cells reached 90–95% confluence, they were transfected with wild-type CaR expression constructs using Lipofectamine 2000^{TM} (Invitrogen). A given amount of plasmid DNA was diluted in Dulbecco's modified Eagle's medium, mixed with diluted Lipofectamine 2000^{TM}, and allowed to complex at room temperature for 20 min before being added to HEK-293 cells in plates.

HEK-293 cells were maintained in 25 cm^2 culture flasks and transfected with 8 μg of the wild-type CaR expression constructs using Lipofectamine 2000^{TM} according to the manufacturer's instructions (Invitrogen). After 24 h, cells were transferred to 24-well plates and grown for a further 24 h. Selection of stable transformants was then carried out in the presence of 100–400 μg mL^{-1} geneticin (Invitrogen). Individual resistant clones were isolated 3 weeks later, screened by aequorin luminescence for activity, and subsequently studied by microfluorimetry using Fura-2 (Mun et al. 2004).

The aequorin luminescence screening assay used to identify CaR-expressing HEK-293 cell clones for further analysis was performed as described previously (Tan et al. 2003). HEK-293 cells that had been transfected with the wild-type CaR were cultured on glass coverslips in Dulbecco's modified Eagle's medium, 10% fetal bovine serum in 6-well plates, and loaded with Fura-2AM (5 μM, 2 h; 37°C) in physiological saline solution containing 125 mM NaCl, 4.0 mM KCl, 1.0 mM $CaCl_2$, 1.0 mM $MgCl_2$, 20 mM HEPES (NaOH, pH 7.45), NaH_2PO_4 0.8 mM, 5.6 mM D-glucose, 1 mg mL^{-1} bovine serum albumin. After 2 h the Fura-2-containing solution was removed, and the cells were resuspended in physiological saline for 30 min at 37°C. The control perifusion solution had the following composition: 125 mM NaCl, 4.0 mM KCl, 0.5 mM $CaCl_2$, 1.0 mM $MgCl_2$, 20 mM HEPES (NaOH), 0.1% D-glucose, pH 7.45. The coverslip was fixed into a perfusion chamber, and perifused with this medium using a Gilson peristaltic pump (Paris, France) at a flow rate of ~1.1 mL min^{-1} with Ca^{2+} concentrations between 0.5 and 10 mM, in the temperature range 12–37°C. Fluorescence excitation was performed using alternating wavelengths (340 and 380 nm), and detection of emitted light at ~510 nm was performed as previously described

(Bradbury et al. 1996). The fluorescent images were recorded on a Zeiss Axiovert 200 M microscope using a monochrome HSm digital camera (Zeiss, Oberkochen, Germany) with a 63× Zeiss long working-distance objective. Region-of-interest excitation ratio data were extracted using Stallion software (Intelligent Imaging Innovations, Denver, CO) and subsequently processed using *Mathematica* (Wolfram Research, Champaign, IL) (Wolfram 2007). Data for cytoplasmic free-Ca^{2+} concentrations were expressed as either uncorrected excitation ratios (340 nm/380 nm) or converted to ionized Ca^{2+} concentration using a calibration procedure. With fluorescence emission detection set at 510 nm, the Fura-2 excitation ratio (340 nm/380 nm) was used as a measure of intracellular $[Ca^{2+}]$. The ratio data obtained were calibrated using the equation (Grynkiewicz et al. 1985)

$$[Ca^{2+}] = K_d \frac{(R - R_{min}) S_{f2}}{(R_{max} - R) S_{b2}}, \quad (1)$$

where $K_d = 224$ nM (dissociation constant for Ca^{2+}/Fura-2 complex), R is the observed fluorescence ratio, R_{min} is the minimum fluorescence ratio, R_{max} is the maximum fluorescence ratio, S_{f2} is the fluorescence reading obtained at 380 nm in the absence of Ca^{2+}, and S_{b2} is the fluorescence reading obtained at 380 nm in the presence of saturating concentrations of Ca^{2+} ions (i.e., ≥100 μM). R_{min} and S_{f2} were estimated using Ca^{2+}-free solution that contained 5 mM EGTA and 2 μM ionomycin. R_{max} and S_{b2} were determined using a solution that contained 2 μM ionomycin, 10 mM $CaCl_2$, and no EGTA.

Theory of methods

Because the wavelet transform is formally derived from the Fourier transform, it is useful to give an outline of the Fourier transform, in the present context.

Fourier transform

The Fourier transform is a linear operator that maps one function of a given independent variable (time) onto another function of a so-called conjugate variable (frequency) (Butz 2006; Bracewell 1999). The Fourier transform decomposes a function into a continuous spectrum of its frequency components, and the inverse transform synthesizes a function from its spectrum of frequency components. Similarly, the discrete Fourier transform maps a time series onto a finite spectrum of its frequency components (Butz 2006; Bracewell 1999).

The Fourier transform of a complex-valued Lebesgue-integrable function, $x(t)$ is defined in discrete-series processing, as the function:

$$X(f) = \int_{-\infty}^{\infty} x(t) e^{-i2\pi ft} dt, \quad (2)$$

for every real number f.

When the independent variable t represents time (with SI unit of seconds), the transform variable f represents ordinary frequency (in Hertz). The complex-valued function, X is said to represent x in the frequency domain, i.e., if x is a continuous function, then it can be reconstructed from X by the inverse transform:

$$x(t) = \int_{-\infty}^{\infty} X(f) e^{i2\pi ft} df, \quad (3)$$

for every real number t, and premultiplied by a scaling parameter that is not given here.

The interpretation of X is aided by expressing it in polar coordinate form:

$$X(f) = A(f) e^{-i\phi(f)}, \quad (4)$$

where

$$A(f) = |X(f)| \quad (5)$$

is the amplitude, and

$$\Phi(f) = \text{Angle}(X(f)) \quad (6)$$

is the phase.

Then the inverse transform can be written:

$$x(t) = \int_{-\infty}^{\infty} A(f) e^{i(2\pi ft + \Phi(f))} df, \quad (7)$$

which is a recombination of all the frequency components of $x(t)$. Each component is a sinusoid expressed in complex form, $e^{i2\pi ft}$, whose amplitude is $A(f)$ and whose initial phase angle (at $t = 0$) is $\Phi(f)$.

Wavelet transform

It is important in many situations, however, to obtain the temporal structure of the frequency content of a time series in a transparent way. One way to obtain both time and frequency localization is to use a windowed Fourier transform. As the name suggests, the signal is multiplied by a window function $b(t - t_0)$, where $b(t)$ is nonzero only in a finite region at and beyond $t = 0$. Then the Fourier transform of $x(t)$ $b(t - t_0)$ is:

$$\hat{X}(f, t_0) = \int_{-\infty}^{\infty} x(t) b(t - t_0) e^{-ift} dt. \quad (8)$$

This gives the frequency content of the signal near $t = t_0$. It is clear that only the signal around $t = t_0$

contributes to $\hat{X}(f, t_0)$, since this is the part of the signal that is "seen" through the window and the rest is cut off by the function $b(t)$. As the window is moved along the time axis, different parts of the signal are seen, and this gives a time-frequency description of $f(t)$.

Generally, a discrete wavelet transform is described as a windowed Fourier transform, where the frequency components of a time series are localized to every temporal region; and it yields a higher level of confidence in the interpretation of the transformed data.

The continuous wavelet transform of a discrete sequence x_n is defined as the convolution of x_n with a scaled and translated version of $\psi_0(t)$, the "mother" wavelet (Torrence and Compo 1998):

$$W_n(s) = \sum_{n'=0}^{N-1} x_{n'} \psi^* \left[\frac{(n' - n)\delta t}{s} \right], \quad (9)$$

where N is the total number of points in the time series, ψ is the mother wavelet function scaled by the real factor s and translated along the localized time index n, δt is the time separation between points in the series; and asterisk denotes the complex conjugate of the respective function. By varying n and s through appropriate ranges, we construct an image showing both the amplitude of any features versus the wavelet scale.

Convolution function

The choice of the mother wavelet, $\psi_0(t)$, is to some extent arbitrary but the particular choice is very important as it determines the features that are enhanced after its convolution with the data. In the present work we used the Morlet wavelet (Goupillaud and Grossman 1984) but there are several well-established wavelet functions from which to choose; the Morlet and derivative of a Gaussian (DOG) wavelets are illustrated in Fig. 2.

Performance testing of wavelet transform

To illustrate the importance of the correct choice of wavelet function, a synthetic time series was created to resemble the structure of the data obtained from our experiments (Fig. 3). The recycle time (δt) was set to 1 Hz and a sinusoidal signal of frequency 0.0625 Hz was applied for an interval of 8 s, followed by a delay of 24 s. This was repeated for 14 min to give a time series with sufficient information to yield a high-resolution Fourier transform. Essentially, this time series is described as a sine wave with a wavelength of 16 s sampled to π radians (half of a wave), with a gap between peaks of 32 s. Note that an increased sample size of a time series does not enhance the resolution of a wavelet transform, however insufficient sample size does limit the number of choices of the wavelet scale, since complete wavelet convolution would not occur in regions of interest if the time interval were too short. If the time series is limited in length, the outcome of the analysis may be improved by postpadding the data with zeroes.

In conclusion, discrete wavelet transform analysis, as shown in Fig. 3, using the advantages of the Morlet wavelet was deemed appropriate to process the data obtained from our microscopy experiments.

We note that this type of analysis allows comment on the temporal stability of the frequency of the oscillator. This is a subject of considerable current interest since a recent model is primarily directed at possible stochastic excitation of the oscillator (Skupin and Falcke 2007). In agreement with this is a recent study which focuses on Fourier-transform-derived data analysis of intracellular Ca^{2+} oscillations in hepatic cells (Perc et al. 2008).

Model design

For the pathways presented in Breitwieser (2006) and Falcke (2004) we devised a system of kinetic equations:

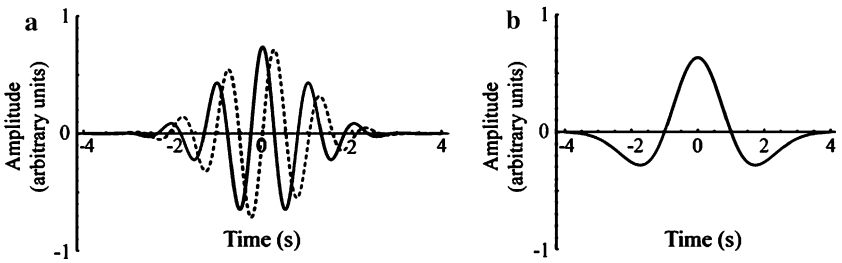

Fig. 2 Two different wavelet bases of both the real (*solid*) and imaginary (*dashed*) parts of (**a**) the Morlet wavelet, whose equation is $\pi^{1/4} e^{i\omega_0 t} e^{-t^2/2}$ with $\omega_0 = 6$, and (**b**), the derivative of a Gaussian (DOG) wavelet, whose equation is $\frac{(-1)^{m+1}}{\sqrt{\Gamma(m+\frac{1}{2})}} \frac{d^m}{dt^m} \left(e^{-\frac{t^2}{2}} \right)$ with $m = 2$. Note that the DOG has no imaginary part, only a real part

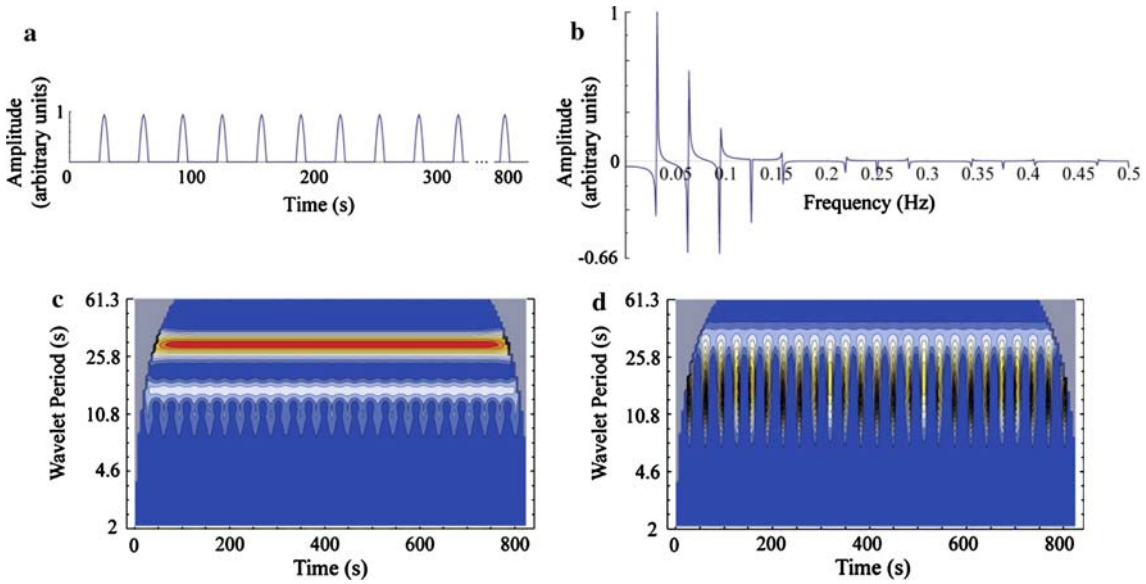

Fig. 3 Tests of performance of Fourier and wavelet transforms on synthetic periodic data. **a** Synthetic time series with 0.0625-Hz sinusoidal half-wave oscillations occurring in bursts every 32 s, **b** Fourier transform, and wavelet transforms of this time series calculated using **c** the Morlet wavelet (with wavelet number 6) and **d** the DOG mother wavelet with the second derivative. *Blue color* in the wavelet transform denotes zero to low power, white denotes midlevel power, and red denotes the maximum power of the signal. The *dull blue* in the top corners delimits the "cone of influence" or the areas of no significance due to incomplete wavelet convolution (Torrence and Compo 1998)

$$
\begin{aligned}
&\xrightarrow{v_1} S_1 + E_1 S_2^{\gamma} \underset{k_{-1}}{\overset{k_1}{\rightleftharpoons}} S_1 E_1 S_2^{\gamma} \\
S_1 E_1 S_2^{\gamma} &\xrightarrow{k_2} S_1 + E_1 S_2^{\gamma} + S_2 \xrightarrow{v_2} \\
&\gamma S_2 + E_1 \underset{k_{-3}}{\overset{k_3}{\rightleftharpoons}} E_1 S_2^{\gamma} \\
&E_2 + S_2 \underset{k_{-4}}{\overset{k_4}{\rightleftharpoons}} E_2 S_2 \\
&S_3 \underset{v_{\mathrm{SERCA}}}{\overset{k_5}{\rightleftharpoons}} S_4 \xrightarrow{\mathrm{PMCA}},
\end{aligned}
\tag{10}
$$

where we interpreted v_1 as the rate with which Ca^{2+} is supplied to the pool of S_1; this represents the extracellular Ca^{2+} concentration that is available to interact with the CaR; E_1 is the CaR; S_2 is the cytoplasmic inositol trisphosphate (IP_3); k_1 and k_{-1} are the rate constants that characterize the equilibration between extracellular Ca^{2+} and Ca^{2+} bound to the CaR; k_2 characterizes the rate of the signaling cascade between Ca^{2+} bound to the CaR and IP_3 formation; v_2 is the rate at which cytoplasmic IP_3 decomposes; k_3 and k_{-3} describe the reaction of the intracellular IP_3 with the CaR; γ is the cooperativity index describing the interaction between IP_3 and the CaR; E_2 is the IP_3R; k_4 and k_{-4} are the rate constants that characterize the equilibration of cytosolic IP_3 and IP_3 bound to the IP_3R; S_3 is Ca^{2+} in the ER; S_4 is the Ca^{2+} in the cytosol; k_5 is the rate constant describing the efflux of Ca^{2+} in the ER to the cytosol; v_{SERCA} represents the Michaelis-Menten equation describing the flux of Ca^{2+} through the endoplasmic reticulum Ca^{2+}-ATPase (SERCA); and v_{PMCA} is the Hill equation describing the flux of Ca^{2+} through the plasma membrane Ca^{2+}-ATPase (PMCA). The fluxes v_{SERCA} and v_{PMCA} are characterized by the following equations:

$$
\begin{aligned}
v_{\mathrm{SERCA}} &= \frac{V_{\mathrm{SERCA}}[S_4]}{K_{\mathrm{SERCA}} + [S_4]} \frac{1}{[S_3]}, \\
v_{\mathrm{PMCA}} &= \frac{V_{\mathrm{PMCA}}[S_4]^{\phi}}{K_{\mathrm{PMCA}} + [S_4]^{\phi}},
\end{aligned}
\tag{11}
$$

where V_{SERCA} and K_{SERCA} are the $V_{\max}$ and K_{M} of the SERCA, respectively; V_{PMCA} and K_{PMCA} are the $V_{\max}$ and K_{M} of the PMCA, respectively; and φ is the Hill coefficient for the PMCA (Albrecht et al. 2002). The term $1/[S_3]$ in v_{SERCA} is included since experimental evidence suggests that the rate of SERCA pumping is negatively modulated by Ca^{2+} in the cytosol (Sneyd et al. 2003).

In combination, these schemes for the induction of the activity of the CaR by extracellular Ca^{2+} give a set of rate equations that describe the evolution of the system in time. Thus, according to the law of mass action and the law of mass conservation (Mulquiney and Kuchel 2003), the reactions in Eq. 10 are described by the set of simultaneous nonlinear differential equations:

$$
\begin{aligned}
[\mathrm{Ca}] &= [\mathrm{Ca_p}],\\
\frac{\mathrm{d}[S_1]}{\mathrm{d}t} &= v_1([\mathrm{Ca}]) - \frac{V_c}{V_e}k_1[S_1][E_1S_2^{\gamma}]\\
&\quad + \frac{V_c}{V_e}k_{-1}[S_1E_1S_2^{\gamma}] - \frac{V_c}{V_e}\rho\frac{V_{\mathrm{PMCA}}[S_4]^{\phi}}{K_{\mathrm{PMCA}}^{\phi} + [S_4]^{\phi}},\\
\frac{\mathrm{d}[S_2]}{\mathrm{d}t} &= k_1[S_1E_1S_2^{\gamma}] - k_3[E_1][S_2]^{\gamma} + \gamma k_{-3}[E_1S_2^{\gamma}]\\
&\quad - v_2([S_2]) + k_{-4}[E_2S_2] - \frac{V_{\mathrm{ER}}}{V_c}k_4[E_2][S_2]\\
\frac{\mathrm{d}[S_3]}{\mathrm{d}t} &= \frac{V_c}{V_{\mathrm{ER}}}\frac{V_{\mathrm{SERCA}}[S_4]}{K_{\mathrm{SERCA}} + [S_4]}\frac{1}{[S_3]} - \beta k_5[S_3]^{\beta}[E_2S_2],\\
\frac{\mathrm{d}[S_4]}{\mathrm{d}t} &= -\frac{V_c}{V_{\mathrm{ER}}}\frac{V_{\mathrm{SERCA}}[S_4]}{K_{\mathrm{SERCA}} + [S_4]}\frac{1}{[S_3]} - \frac{V_{\mathrm{PMCA}}[S_4]^{\phi}}{K_{\mathrm{PMCA}}^{\phi} + [S_4]^{\phi}}\\
&\quad + \frac{V_{\mathrm{ER}}}{V_c}\beta k_5[S_3]^{\beta}[E_2S_2],\\
\frac{\mathrm{d}[E_1S_2^{\gamma}]}{\mathrm{d}t} &= -\frac{V_e}{V_c}k_1[S_1][E_1S_2^{\gamma}] + (k_{-1} + k_2)[S_1E_1S_2^{\gamma}]\\
&\quad + k_3[E_1][S_2]^{\gamma} - k_{-3}[E_1S_2^{\gamma}],\\
\frac{\mathrm{d}[S_1E_1S_2^{\gamma}]}{\mathrm{d}t} &= \frac{V_e}{V_c}k_1[S_1][E_1S_2^{\gamma}] - (k_{-1} + k_2)[S_1E_1S_2^{\gamma}],\\
\frac{\mathrm{d}[E_2S_2]}{\mathrm{d}t} &= -\frac{V_c}{V_{\mathrm{ER}}}k_{-4}[E_2S_2][S_4] + \frac{V_c}{V_{\mathrm{ER}}}k_4[E_2][S_2],\\
\frac{\mathrm{d}[E_1]}{\mathrm{d}t} &= -k_3[E_1][S_2]^{\gamma} + k_{-3}[E_1S_2^{\gamma}],\\
\frac{\mathrm{d}[E_2]}{\mathrm{d}t} &= k_{-4}[E_2S_2] - \frac{V_c}{V_{\mathrm{ER}}}k_4[E_4][S_2],
\end{aligned}
\tag{12}
$$

where t is time; [Ca] is the concentration of the pool of extracellular Ca^{2+}; $[Ca_p]$ is the concentration of the perfused Ca^{2+} (highly buffered); $[S_1]$ is the concentration of the fraction of extracellular Ca^{2+} available for interaction with the CaR; $[S_2]$ is the concentration of cytoplasmic IP_3; $[S_3]$ is the concentration of Ca^{2+} in the ER; $[S_4]$ is the concentration of Ca^{2+} in the cytosol; $[E_1]$ is the concentration of free CaR; $[E_2]$ is the concentration of free IP_3R; V_c is the cytoplasmic volume fraction; V_e is the extracellular volume fraction; V_{ER} is the ER volume fraction; γ is the cooperativity index; β is a stoichiometry coefficient; and ρ is the fraction of extruded Ca^{2+} available to interact with the CaR. Figure 4 shows how this system of equations relates to the reactions shown in Fig. 1.

By substitution of a consistent set of parameters, in accordance with previous work (Sneyd et al. 2003; Mulquiney and Kuchel 2003), the system produced an oscillatory signal for the key dependent variables, most notably $[S_4]$.

The scheme produced oscillations in its solution similar to those that we obtained experimentally. To gain control of the frequency of the oscillations, we used a scalar that affects all of the rate constants and V_{max} values, and included a logistic equation into the expression for v_1 to take into account the critical threshold Ca^{2+} concentration, below which oscillations ceased; this was estimated experimentally. Details of the *Mathematica* program are given in Appendix 1.

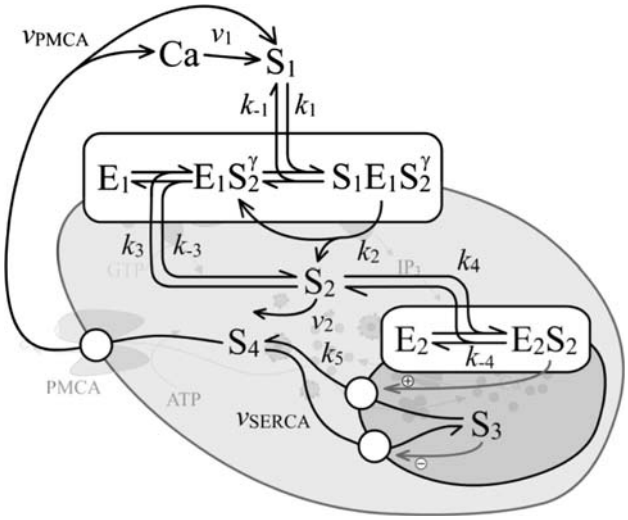

Fig. 4 Mapping of the pathways for CaR-mediated induction of intracellular Ca^{2+} oscillations onto the kinetic model given in Eq. 10. See text for definitions of the components of the reaction scheme

We considered the system from a purely enzyme kinetic standpoint, and showed that the observed oscillations could be simulated with a reaction scheme based on key biochemical features (Breitwieser 2006; Falcke 2004). This enabled the fitting of values of rate constants, and identification of those reactions which most affected the frequency and form of peaks in the time courses. Thus, we did not consider spatial diffusion in our deterministic model since our methodology was not aimed at this aspect of the behavior of the oscillator.

Results

Images

Exposure of Fura-2-loaded HEK-293 cells to Ca^{2+} concentrations >0.5 mM had a significant effect on cytoplasmic free-Ca^{2+} concentration, as inferred from the images obtained with fluorescence microscopy. Figure 5 shows the digitized camera view of a typical light, and fluorescence, microscopy experiment on ~50 HEK-293 cells using a 40× objective. Artifactual halos surround the cells in Fig. 5a; they are typical of phase-contrast microscopy of these live cells. Figure 5b shows a typical example of Fura-2 fluorescence signals from a population of cells.

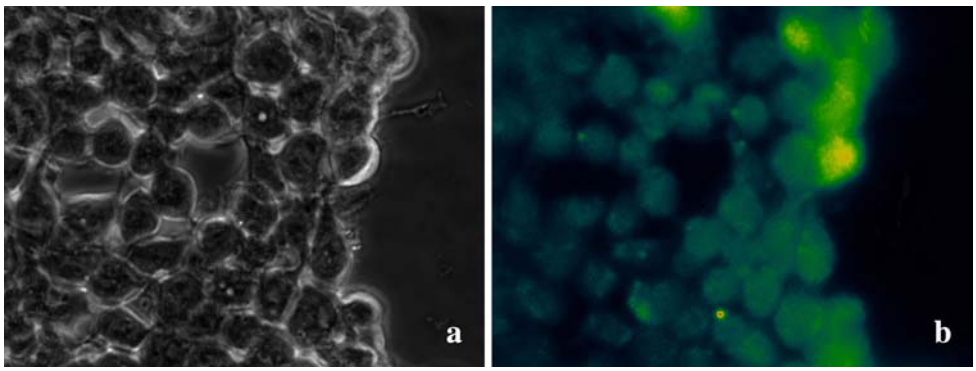

Fig. 5 Light micrographs (using a 40× objective) of HEK-CaR cells using: **a** phase-contrast microscopy and **b** Fura-2 fluorescence microscopy with excitation at a wavelength of 380 nm and detection at 510 nm. Fluorescence intensity of 3 × 3 and 4 × 4 central voxels yielded time courses such as the one shown in Fig. 6

Experimental data

Figure 6a–c shows the oscillatory nature of the Fura-2 fluorescence ratio; the oscillation frequency decreased very distinctly as the temperature was decreased. This response was reflected in the windowed Fourier transforms shown in Fig. 6d–f. Since the oscillatory data were on an elevated baseline, the zero-frequency component was substantially greater in amplitude than for other peaks; they were therefore excised when drawing Fig. 6d–f. "Sinc wiggles" that are characteristic of the Fourier transform of data sets that are truncated at nonzero amplitudes, were present, as

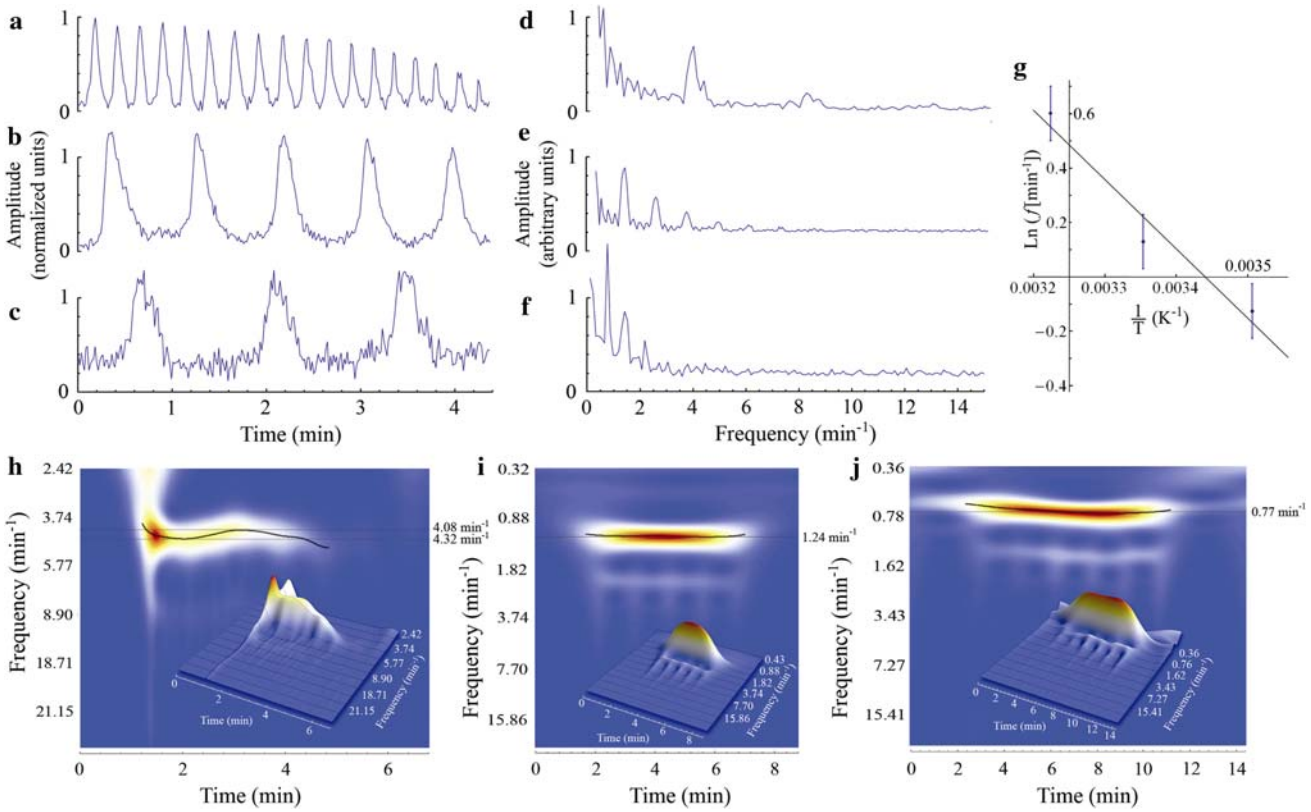

Fig. 6 Processed data from Fura-2 intensity measurements from HEK-293 cells. **a–c** Ratiometric (340/380 nm) fluorescence microscopy data from HEK-293 cells perifused with 5 mM Ca^{2+} at 37°C, 25°C, and 12°C, respectively; their Fourier transforms, **d–f**, show predominant peaks at ~4.1, ~1.35, and ~0.75 min^{-1}, respectively (note, the ordinate has arbitrary fluorescence intensity values); **h–j** their corresponding 2D wavelet transforms with 3D wavelet transform (inset) with local transform maxima highlighted by the *thick black line*. *Red color* denotes maximal wavelet power, *white color* denotes medium power, and *blue color* denotes zero to low wavelet power. Data used for wavelet transforms were padded with zeros on both sides to ensure complete wavelet convolution. **g** Arrhenius plot for the data in **a–c**, with slope −2550 corresponding to an apparent activation energy for the frequency of 21.2 kJ mol^{-1}. *Error bars* denote a coefficient of variation of 10%. The estimate of the apparent activation energy was used in the function tempScalar in the model in Appendix 1

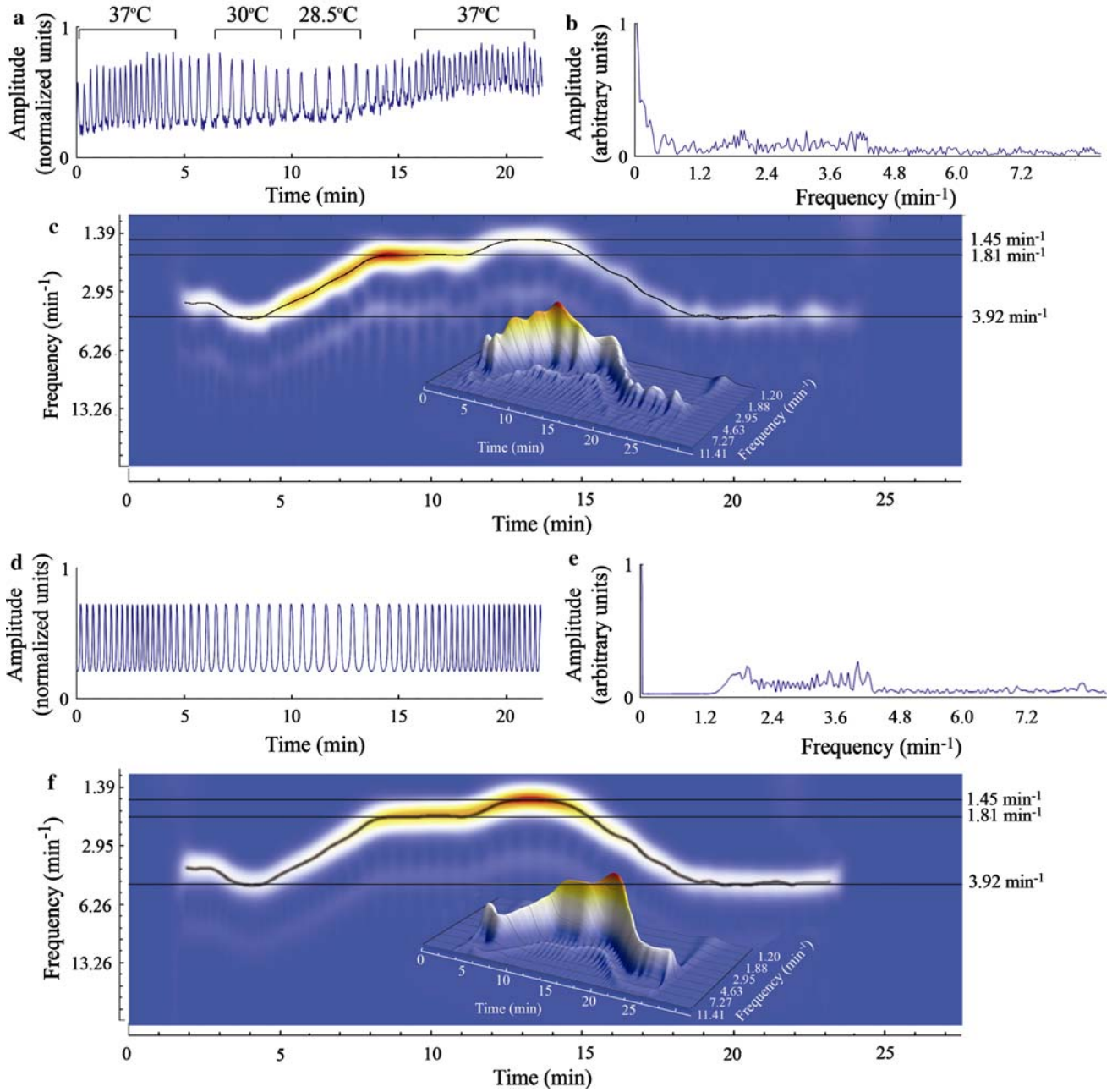

Fig. 7 **a**–**c** Processed data from Fura-2 intensity measurements from HEK-293 cells, **d**–**f** corresponding simulated data. **a** Ratiometric (340 nm/380 nm) fluorescence microscopy data from HEK-293 cells perifused with 5 mM Ca^{2+}. At 3.5 min, the temperature was reduced from 37°C to ~30°C, and at 11 min, it was further reduced to 28.5°C. At 14 min, the temperature was returned to 37°C. **b** Fourier and **c** two dimensional wavelet transform with 3D wavelet transform (inset) of these data. The local maxima at each time point through the time course are highlighted by the *curved black line* and the frequencies at which the oscillations remained stable for extended periods are highlighted by the *horizontal black lines* at 1.45, 1.81, and 3.92 min^{-1}. **d** Numerical solution of $S_2(t)$, where the temperature is calculated from the local maximum at each time point of the wavelet transform in (**c**); **e** Its Fourier transform, and **f** its 2D wavelet transform and 3D wavelet transform (*inset*). The local maximum of frequency at each time point through the time course is highlighted by the *curved black line*

well as artifactual harmonic peaks of approximately half the intensity of each previous peak. Evident, particularly in Fig. 6d, was a subtle change in frequency over the windowed time course from the slightly skewed line with a shoulder peak, representing a frequency range of ~3.9–4.5 min^{-1}. The wavelet transforms (Fig. 6h–j) showed similar results, but the change in frequency over time was more easily seen and was temporally well localized.

We estimated an activation energy of 21.2 kJ mol^{-1} from the Arrhenius plot from Fig. 6g, which is moderately

Table 1 Rate constants for the kinetic model of the CaR pathway (Fig. 4) at 37°C

K_{PMCA}	0.425 μM	k_1	3.741 mol^{-1} L s^{-1}
V_{PMCA}	28 μM s^{-1}	k_{-1}	115.22 s^{-1}
K_{SERCA}	0.18 μM	k_2	53.54 s^{-1}
V_{SERCA}	120 μM s^{-1}	k_3	1.007 mol^{-3} L^3 s^{-1}
β	0.4	k_{-3}	18.1 s^{-1}
γ	3	k_4	58.35×10^{-3} mol^{-1} L s^{-1}
ϕ	2	k_{-4}	633.01 s^{-1}
ρ	0.1	k_5	500 s^{-1}
v_1*	7.63×10^{-4} mol L^{-1} s^{-1}		
v_2	53.54 mol L^{-1} s^{-1}		

* indicates that a logistic function was used to simulate the critical threshold extracellular Ca^{2+} concentration required for oscillations in intracellular Ca^{2+} concentration

Table 2 Control coefficients, where parameter is denoted by p and frequency by f, calculated using Eq. 13 with $\Delta p = 0.95 p_{norm}$, for some of the rate constants given in Table 1 and the [CaR] at 37°C

k_1	1.69
k_{-1}	−1.16
k_2	−0.562
k_3	1.57
k_{-3}	−2.21
v_1	5.70
v_2	−5.58
$[CaR]_{total}$	0.040

Large perturbations in the rate constants k_4, k_{-4}, and k_5 and the velocities v_{SERCA} and v_{PMCA} did not significantly affect the oscillation frequency

lower than the activation energy for water transport in human red blood cells (~25 kJ mol^{-1}) (Benga et al. 1987). This seems reasonable since, like water in red blood cells, Ca^{2+} is transported via membrane proteins, but unlike water, Ca^{2+} cannot form hydrogen bonds with the transporter, which could explain its slightly lower activation energy.

To demonstrate the efficacy of applying the wavelet transform to data recorded from cells in which there was a clear change in frequency, HEK-293 cells were exposed to 5 mM Ca^{2+} at time-varying temperatures. Figure 7b and c show the resulting Fourier and wavelet transformation, respectively, from HEK-293 cells where the temperature of the perfusion solution had been changed over time, while oscillations in Fura-2 fluorescence intensity are given in Fig. 7a. The Fourier transform showed weak signals in the range of frequencies between 1.4 and 4.2 min^{-1}, however the signal-to-noise ratio was low. The wavelet transform showed remarkably well-resolved peaks in wavelet power that correlated highly with expected frequencies over the temporal domain.

Figure 7d shows the time course from a simulated experiment using the temperatures estimated to form the curved black line in Fig. 7c. Its corresponding Fourier and wavelet transformation are shown in Fig. 7e and f. The features of the simulated time course are very close to the experimental data shown in Fig. 7a, with a relatively high frequency at the beginning, a gradual decrease in frequency approaching the middle, and an increase in frequency at the end. The Fourier and wavelet transforms also contained all the features of the experimental data transforms, respectively, except there was no red-noise component of the Fourier transform, and the amplitude in the wavelet transform was more uniform over time. This is a consequence of the absence of noise in the synthetic data, and the signal in the simulated transform was not diminishing, unlike in the real experimental data.

Model fitting and performance

In our model, the reversible catalytic cycle was composed of the following reactions: (1) binding of Ca^{2+} to the CaR from the extracellular side of the cellular membrane; (2) a signaling cascade leading to the production of IP_3; (3) feedback from the released IP_3 to the CaR and binding to the IP_3R, or activation of the CaR arising from the simultaneous activation of protein kinase C (PKC); and (4) stimulation of the ER-Ca^{2+} channel, leading to the extrusion of Ca^{2+} into the cytoplasm and extracellular fluid.

Experimental data were recorded as described above, and used to determine values of rate constants by manual iteration of parameter values (Table 1); the corresponding control coefficients of the parameters are given in Table 2. We estimated these control coefficients using the following equality, by analogy with the coefficients of metabolic control analysis (Mulquiney and Kuchel 2003; Heinrich and Schuster 1996):

$$C_p^f = \left(\frac{\partial \ln f}{\partial \ln p}\right)_{\text{norm}} = \frac{P_{\text{norm}}}{f_{\text{norm}}}\left(\frac{\partial f}{\partial p}\right)_{\text{norm}} \cong \frac{P_{\text{norm}}}{f_{\text{norm}}}\left(\frac{\Delta f}{\Delta p}\right)_{\text{norm}}, \quad (13)$$

where f is the frequency of oscillations produced by the system, p is the parameter being perturbed, and the subscript "norm" denotes the corresponding normal (steady-state) value in the system. This expression produces a measure of the influence that each parameter has on the frequency of the oscillating system. The numerical solution of the function $S_3(t)$ for different temperature values is given in Fig. 8. Limit cycles of combinations of analyte concentrations were also computed (Fig. 9) to show that this nonlinear dynamical system was stable at $t \to \infty$, and to determine the character and phase relationships between these analytes.

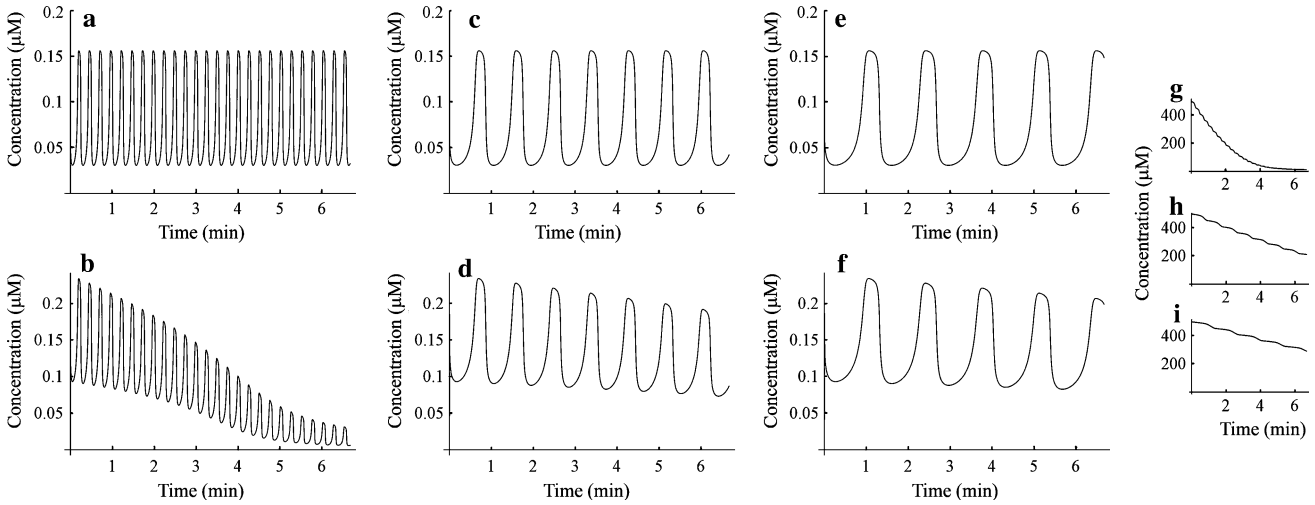

Fig. 8 Numerical solution of the functions $S_2(t)$ (IP_3, **a**, **c**, **e**); $S_3(t)$ (ER Ca^{2+}, **g**, **h**, **i**); and $S_4(t)$ (intracellular Ca^{2+} **b**, **d**, **f**) in Eq. 12. The values of the rate constants used are given in Table 1. These were multiplied by a scalar quantity whose value was the solution of the exponential equation: $0.173 + 1.61 \times 10^{-3}\ e^{0.1684T}$, where T is the desired temperature in degrees Celsius, which was set to (**a**, **b**, **g**) 37°C, (**c**, **d**, **h**) 25°C, and (**e**, **f**, **i**) 12°C. The value of the scaling factor (relating fluorescence intensity to concentration of free Ca^{2+}) was determined experimentally

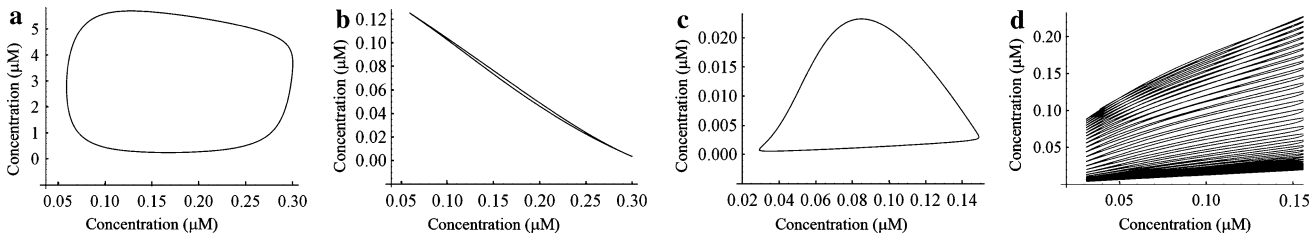

Fig. 9 Limit cycles of the oscillations produced by analytes in the system described by Eq. 12, with temperature at 37°C. Perfused $[Ca^{2+}]$ was set to 5 mM, and the numerical solutions sampled from $t = 20$ s to 10,000 s in 0.01 s increments. **a** $[S_2]$ versus $[S_1]$, **b** $[S_2]$ versus $[E_1]$, **c** $[S_1E_1S_2^{\gamma}]$ versus $[E_1S_2^{\gamma}]$, and **d** $[S_2]$ versus $[S_4]$. The *limit cycles* show sustained oscillations for each of the tested analytes, except $[S_4]$ which diminished due to the emptying of the ER stores during the time course (Fig. 7g)

Discussion

Wavelet transform performance

Synthetic data

The Fourier transform of synthetic oscillatory data (Fig. 3) showed dispersive peaks at 0.03125 and at 0.0625 Hz with an artifactual harmonic peak at ~0.1 Hz, and many other frequencies. The most noticeable difference between the images was the fine-scale structure in the DOG wavelet transform. This arose because the DOG wavelet is real-valued and it captures both the positive and negative oscillations of the time series as separate peaks in wavelet power. The Morlet wavelet is a complex function, and the corresponding data analysis contains more oscillations than the DOG wavelet, and hence the wavelet power combines both positive and negative peaks into a single, broad peak. This feature of the Morlet wavelet transform was highly advantageous when processing the data that we acquired, since there was a continuous high-power peak at ~32 s (0.03125 Hz) and peaks of midlevel intermittent power at ~16 s (0.0625 Hz). Note that this peak was unbroken over the whole time domain. Harmonic peaks occurred at ~10 s (0.1 Hz), but these were of low power and had gaps of zero power between them, making them easily discernible from the authentic peaks in the transform.

The DOG wavelet transform produced an image with high-power intermittent peaks of 16-s period and a low-power continuous 32-s-period peak, however the peaks were far smoother over a range of periods than with the Morlet wavelet transform, but were sharper over broader domains of time.

Wavelet transforms have the valuable attribute of being able to be computed with standard functions in various common computing environments, such as *Mathematica*. To compute the wavelet transform of a time series $x(t)$, we first chose appropriate wavelet time scales:

$$\sum_{j=0}^{m} 2\delta t \times 2^{j\delta j}, \tag{14}$$

where δt is the period between successive time points; j denotes the scale number, ranging from 0 to m, the desired number of scales; and δj is the difference between successive scales. We initially chose $j = 60$ s, and $\delta j = 0.125$ s, for a minimum and maximum wavelet scale of $\sim$1.84 s and $\sim$333 s, respectively. To approximate the continuous wavelet transform, the convolution equation (Eq. 9) should be applied N times for each scale, where N is the number of points in the time series (Kaiser 1994). To save computation time we used the fact that the convolution theorem allows all N convolutions simultaneously in Fourier space (Eq. 2) (Butz 2006). Evaluation of the wavelet transform is then:

$$W_{\mathrm{n}}(s) = \sum_{j=1}^{n} X(f)\Psi \times (sf)\mathrm{e}^{\mathrm{i}fn\mathrm{d}t}, \tag{15}$$

where Ψ is the Fourier transform of the mother wavelet. An explanation of how this was achieved in *Mathematica* is given in Appendix 1.

Experimental data

The wavelet transform of the experimental data in Fig. 6h–j shows the stability of the frequency over time and the potential for detecting subtle changes. We note that, especially for cells at 25°C, the frequency was extremely stable over the 6-min time course (Fig. 6i); this is in contradistinction to recent suggestions for stochastic excitation of the oscillator (Skupin and Falcke 2007; Perc et al. 2008). Frequency variations of the system at 37°C (Fig. 6h) are postulated to have been due to slight instability of the thermostat and heat sink.

Wavelet analysis is ideal for Ca^{2+} oscillation experiments since long time courses can be processed without the need for a window function; it also provides clear estimates of the stability of the frequency, making it useful for studying systems which are described by stochastic variables. The processing time required was subsequently much greater since the product of the inverse Fourier transform of the input data, and an evaluation of the Morlet wavelet, were taken for each specified wavelet scale. Depending on the number of data points and the desired number of scales, the processing time was of the order of several seconds to several minutes, while the processing time for the fast Fourier transform was negligible. Temporal resolution is also an important consideration; while the range of wavelengths (periods) in both transforms is $0 - \delta t/2$, the number of uniquely represented wavelengths in the Fourier transform is constrained to $N/2$, where N is the number of data points. The number of wavelengths represented in the wavelet transform can be increased by increasing the number of wavelet scales.

The wavelet transform given in Fig. 7c shows how powerful this analytical tool can be when applied to appropriate data. Note again that the periods for which the temperature was stable had oscillations of a stable frequency. The wavelet power throughout the time course was significantly higher than the background noise, and temporal changes in oscillation frequency could easily be traced; and in this example, the oscillator frequency could be used as a cellular thermometer. The curved black line follows the local maximum at each value of t, while the frequencies at which the cells remained stable for extended periods are highlighted with the horizontal black lines in Fig. 7c and f. In stark contrast, the Fourier transform of the same data set gave very little information on fluctuations of the oscillation frequency. The range of frequencies between 1.4 and 4.2 min^{-1} all had approximately the same power and many of the peaks were almost indistinguishable from the background noise.

Conclusion

In summary, the results obtained from the wavelet transform of Ca^{2+} experimental data on Ca^{2+}-induced fluorescence from CaR-expressing HEK-293 cells exposed to variations in extracellular Ca^{2+} concentration, and temperature, were in excellent agreement with previously published results (Baker et al. 2002). These data were used to determine empirically (by visual fitting) the parameter values for use in the model. The wavelet transform was ideal for the analysis of our experiments since time courses lasting for 30 min or more could be studied without the need to choose a window function for the Fourier transform.

Critique of models of Ca^{2+} oscillations

General

A mathematical model constitutes an important tool in an attempt to summarize data and explain the role of the various components of a system. It has been suggested that the CaR may regulate intracellular Ca^{2+}, thereby affecting capacitative calcium entry (Putney 1986). The conclusions from our experimental results support the idea that signaling within the ER involves interactions between ER Ca^{2+} binding proteins and other components of the CaR signaling system. It has been hypothesized that IP_3 is the causal factor of oscillations (Sneyd et al. 2003; Baker et al. 2002), and through the cyclical phosphorylation/dephosphorylation of PKC (Young et al. 2002), which was shown to be required for oscillations in cytosolic [Ca^{2+}] (PKC is activated by

diacylglycerol, a byproduct of IP_3 formation by phospholipase C (Kamp and Hell 2000), and cytosolic Ca^{2+}) (Young and Rozengurt 2002). There appears to be a consensus that oscillations are caused by a reaction in between the extracellular Ca^{2+} binding to the CaR and the production of IP_3. This is a central feature of our model of the system (Breitwieser 2006; Sneyd et al. 2003; Breitwieser and Gama 2001; Falcke 2004; Young et al. 2002; Young and Rozengurt 2002).

Our model consists of Ca^{2+} binding to the CaR that induces a cellular signal that leads to the production of IP_3, which binds to IP_3R causing the release of intracellular Ca^{2+}, which is then exported from the cell. As noted above, values of rate constants were taken from the literature or were determined empirically. The resulting numerical solution of the differential equations in Eq. 12 gave, amongst all the dependent variables, the concentration of intracellular Ca^{2+}. This was an oscillating signal, similar in frequency and form to the Fura-2 signal observed in the microscope experiments.

There has been recent debate over whether [Ca^{2+}] oscillations should be modeled with kinetic rate (deterministic) equations, or with a stochastic approach (Skupin and Falcke 2007; Perc et al. 2006; Gosak et al. 2008). The proposed model defined by Eq. 12 provided good qualitative agreement with our experimental findings. However it is noted that previous experimental data sets appeared to have been burdened with noise, so a stochastic approach was valid when building the models. On the other hand, we considered that the signal-to-noise in our experimental traces was at a level that seemed appropriate for simulations with deterministic equations. This method, when applicable, is more transparent with respect to how the different constituents of the model interact with each other. In other words, a deterministic model allows the application of metabolic control analysis (Mulquiney and Kuchel 2003; Heinrich and Schuster 1996) with its rich predictive power regarding sites that most influence the behavior of a reaction scheme.

Model development

To show how our model related to Fig. 1, we devised a mapping of the system of equations (Eq. 12) onto these pathways; this is given in Fig. 4. The extracellular Ca^{2+} pool, represented by Ca, is supplied to the fraction of extracellular Ca^{2+} (S_1) that is able to bind the CaR, at a rate of v_1. S_1 binds to the receptor with a rate constant of k_1; the complex formed is $S_1E_1S_2^{\gamma}$. This in turn liberates IP_3, represented by S_2, at a rate characterized by k_2. S_2 then either decomposes via v_2, or is recycled via the k_3 reaction; the latter is linked to the formation of $E_1S_2^{\gamma}$, which is in equilibrium with unbound receptor E_1, or binds to the IP_3R (E_2) to form E_2S_2, which is in equilibrium with unbound E_2, via the k_4 reaction. The rate constant, k_2, applies to a reaction that encapsulates much of the signaling pathway leading to the release of IP_3 to the cytoplasm. Upon the formation of E_2S_2, the reaction characterized by the rate constant k_5 is stimulated, and Ca^{2+} from the ER (S_3) is released into the cytoplasm (S_4). S_4 is then either extruded out of the cell through the PMCA or repackaged into the ER through the SERCA at a rate characterized by Eq. 11.

Simulations

Numerical solutions for $S_2(t)$, $S_3(t)$, and $S_4(t)$ with different temperatures are given in Fig. 8. Figure 8a and b show the numerical solutions for S_2 ([IP_3]) and S_4 (cytoplasmic [Ca^{2+}]), respectively, with the system at 37°C, with an oscillation frequency of 4 min^{-1}. The signal from S_4 diminished with a 50% loss of signal after ~4.5 min, and 75% loss after ~6 min. Figure 8c–f shows data from the same system at 25°C and 12°C, with oscillation frequencies of 1.1 and 0.72 min^{-1}, respectively. Figure 8g–i shows the signal from S_3 ([Ca^{2+}] in the ER) at 37°C, 25°C, and 12°C, respectively. (The rate constants were chosen so that the oscillations given, rather than being purely sinusoidal or Lorentzian in amplitude, have a steep increase in intensity, a short sustained peak, and then a gradual decay, to a baseline that is slightly higher than 0.0). The oscillations produced by the system of equations closely approximated those seen in the real experimental data.

Control coefficients

The control coefficients C_p^f, were calculated using Eq. 13, with a decrement of 5% for each parameter. Negative values indicated that the change in oscillation frequency was inversely correlated to the change in parameter value. The values given in Table 2 show that the system's oscillation frequency was more strongly influenced by perturbations in v_1 than any other parameters. This is deemed to be due to the fact that Ca^{2+} is supplied to the system through S_1 via k_1, which is relatively high; thus the steady-state concentration of S_1 is relatively low in spite of the high flux through this pool. This leads to the prediction that, in future experiments, attention might be focused on perturbing the oscillation frequency via conditions which either increase v_1 or decrease k_1. This may include reducing the apparent diffusion coefficient in the extracellular compartment by using a high-viscosity medium. The rate constant v_2 also has a high control coefficient; in other words it has a lot of control over the frequency of oscillations. Conversely, k_{-1} has a relatively low control coefficient since k_1, which describes the reverse reaction, is ~30× the magnitude of

k_{-1}. Interestingly, $[CaR]_{total}$ has the lowest control coefficient of all the tested parameters, indicating a very low influence on the oscillation frequency. The control coefficients of k_4, k_{-4}, and k_5 were all similar and negligible.

The other parameter with a relatively large control coefficient is v_2; this negatively affects the frequency. It characterizes the degradation of IP_3. Our analysis suggests that factors that enhance IP_3 degradation would decrease the frequency of the oscillations. Experimentally this may include pharmacological agents that stimulate phosphatase activity; conversely, phosphatase inhibitors would be predicted to increase the frequency of oscillation.

Knowledge of control coefficients allows rapid insights into those parameters whose perturbation will affect the form and frequency of the oscillating data traces.

Limit cycles

The limit cycles given in Fig. 9 show that the system produced sustained oscillations since there was no decay over the relatively large period of the simulation. Figure 9a shows that the oscillations in $[S_2]$ were $\sim\pi/2$ radians out of phase with $[S_1]$, while Fig. 9b, having a slope going down from left to right, is $\sim\pi$ radians out of phase with $[E_1]$. The former is due mainly to the fact that accumulation of $[E_1S_2^{\gamma}]$ was slow since $[S_2]$ was needed to form this complex, thus allowing S_1 to accumulate. Over time, $[S_1E_1S_2^{\gamma}]$ became relatively high and sufficient amounts of S_2 were released from the complex via k_2. This accounts for the rounded shape seen in Fig. 9a. The latter came about because $[E_1]$ increased, via k_{-3}, from $E_1S_2^{\gamma}$, which could only accumulate at the expense of S_2; in other words, $[E_1]$ increased only as $[S_2]$ decreased, making them out of phase, and producing a limit cycle with the appearance of a diagonal line. The unusual appearance of the limit cycle mapping the relationship between $[S_1E_1S_2^{\gamma}]$ and $[E_1S_2^{\gamma}]$ (Fig. 9c) arises because the shape of the peaks of concentration produced by the two were vastly different. The peaks produced by $[S_1E_1S_2^{\gamma}]$ were much like those computed for $[S_2]$, while those produced by $[E_1S_2^{\gamma}]$ were similar to a Lorentzian curve. They were out of phase by $\sim-\pi/4$ radians since $[S_1E_1S_2^{\gamma}]$ is produced more rapidly as a result of the accumulation of S_1 and the relatively high k_1.

Figure 9d shows that $[IP_3]$ and cytoplasmic $[Ca^{2+}]$ were in phase, having a slope going down from right to left. This was surmised to be because Ca^{2+} efflux from the ER to the cytosol is tightly linked to $[IP_3]$, since the rate constant k_5 is activated only in the presence of IP_3. It also shows that, while the average $[IP_3]$ remained constant, intracellular $[Ca^{2+}]$ slowly diminished. This is shown in Fig. 8 to be due to the ER $[Ca^{2+}]$ approaching 0.0 μM at $\sim$6 min. Figure 9 shows that IP_3 oscillations were sustained regardless of the ER $[Ca^{2+}]$. As a consequence, the model predicts that the Ca^{2+} stores in the ER ultimately become fully depleted. The extent to which this occurs under experimental conditions has not been fully explored; however the decline in the amplitude in the oscillations is consistent with this phenomenon. It is noted that the model does not have an explicit inclusion of inward flux of Ca^{2+}. This is consistent with no increased fluorescence during the perifusion experiments.

An alternative view is that influx was less than efflux, but in the interests of a minimalist model, we consider a situation where an inward flux is zero. Restoration of normal $[Ca^{2+}]$ in the ER could be achieved through a membrane-inserted transporter which is activated upon low ER $[Ca^{2+}]$, but characterization of this pathway has been elusive in the literature.

Breitwieser (2006) shows that transient receptor potential cation channel, subfamily C, member 1 (TRPC1, a membrane Ca^{2+} pore) is recruited by the CaR sensing phenylalanine in the presence of Ca^{2+} (Fig. 1). However, inclusion of this pathway was beyond the scope of the present work, and may be the subject of future studies. Notwithstanding this limitation, our model provides quantitative experiment-prediction capability and describes (simulates) the complicated experiment in which temperature was varied over time with possible adjustment of perifused $[Ca^{2+}]$ (Fig. 7d).

Figure 9a shows that S_1, the population of Ca^{2+} available to interact with the CaR, fluctuates between 1 and 5 μM. This is consistent with a small population of Ca^{2+} that is localized in close proximity to the cell membrane. The concentration of this population fluctuates because a large proportion of it transiently binds to the CaR.

The information provided by the limit cycles gives unique and invaluable insights into the relationships between the different analytes. Figure 9b, for instance, gives the important insight that S_2 and E_1 are highly competitive, and to build onto this model, this competition will have to be preserved.

Overview

In summary, we have developed a robust analytical model capable of predicting and confirming the outcome of experiments where normal conditions have been perturbed. We performed several simulated perturbations including: (1) doubling the [CaR], resulting in a fivefold increase in oscillation frequency, a heightened baseline, and a threefold decrease in oscillation amplitude; (2) halving the [CaR], which suppressed oscillations; and (3) decreasing the initial $[IP_3]$, which caused a long lag period, followed by a period of non-oscillatory Ca^{2+} release, and then normal oscillations. These predictions are all available for further experimental verification.

The current model is a step towards one that might be used in combination with a high-throughput screening approach to determine the physiological outcome of genetically altered cells, where specific signaling mechanisms are addressed. Most importantly, robust models constructed and developed with experimental data will allow prediction of the time dependence of intra- and extracellular signals and how they are decoded to effect cellular responses.

As stated in the "Introduction", previous literature has examined the Ca^{2+}-induced Ca^{2+} release system in various cell types, including parotid acinar cells (Sneyd et al. 2003), HeLa cells (Fioretti et al. 2005), hepatocytes (Baker et al. 2002), normal rat kidney cells (Hofer 1999), and non-excitable cells in general (Fioretti et al. 2005). To our knowledge, ours is the first work in which Ca^{2+} oscillations had been modeled in HEK-293 cells. In constructing and executing our model, we have not: (1) omitted any of the components of the system, such as intracellular stores (Sneyd et al. 2003; Fioretti et al. 2005) and cyclical production of IP_3 (Fioretti et al. 2005; Kusters et al. 2007) which is currently believed to cause the oscillations (Breitwieser 2006; Sneyd et al. 2003); (2) used a time-dependent on/off mechanism to elicit oscillations from the SERCA (Baker et al. 2002); (3) omitted details about the programming of the model, thereby prohibiting its reproduction (Baker et al. 2002; Hofer 1999); (4) used specialized software to produce the model from previous experimental data, and drawn conclusions from the goodness of fit onto these data (Baker et al. 2002); (5) made predictions about the foundations of the system using simulated data from the model (Fioretti et al. 2005; Baker et al. 2002; Hofer 1999); or (6) separated the model into two components, namely flux through the membrane and oscillations in the cytosolic Ca^{2+} (Hofer 1999).

Our presentation here is unique in that we include experimental data which we used to formulate a model as well as the complete program for execution and modification in *Mathematica*. Moreover, we explicitly show how the kinetic equations used to construct the model relate to the current view of the pathways in HEK-CaR cells (Breitwieser 2006; Skupin and Falcke 2007) (Fig. 4). We aimed to construct the model in the simplest possible way using enzyme kinetics to avoid generating myriad parameters and equations which could be fitted to virtually any experimental data. Furthermore, the reader will be able to easily program the model into *Mathematica*, and modify or extend it to suit various applications.

Extensions to the model may include an analysis of the bifurcation properties, and inclusion of membrane potential contributions.

In the present work, we used an approach to analyze the oscillations produced by the HEK-CaR system, and demonstrated that wavelet analysis is superior in many respects to traditional Fourier-transform methods. We showed this through experimental results in which temperature was varied over time, causing a change in oscillation frequency which the wavelet transform method was able to handle in a far more robust way than the Fourier transform of the same data. The main biological conclusion from the work is that oscillations in the concentration of cytoplasmic Ca^{2+} in HEK-293 cells are under the master control of extracellular Ca^{2+} concentration, and the frequency is most affected by the binding of Ca^{2+} to the receptor, and the rate of decay of IP_3.

Acknowledgments For this work, P.W.K. thanks the Australian Research Council for a Discovery Project grant and A.D.C. thanks the Australian National Health and Medical Research Council for a project grant. Dr. Michael Breakspear is thanked for expert advice on wavelet analysis. D.S. thanks the University of Sydney for a Postgraduate Award, and S.C.B. acknowledges a University of Sydney PhD Scholarship.

Appendix

Appendix 1

Mathematica program that solves the array of differential equations given in Eq. 12 to simulate the oscillations in Ca^{2+} concentration in HEK-293 cells.

caConc = 5,000; (* Ca^{2+} concentration in μ mol L^{-1} *)
temp = 37; (* Temperature of the system in Celsius *)
tempScalar = $0.173 + 0.00160882 \times e^{0.1684\,\text{temp}}$; (* Scalar value to account for frequency changes affected by temperature *)
$V_c = 0.33$; $V_{ER} = 0.33$; $V_e = 0.33$; (* Cytosolic, ER, and extracellular volume ratios *)
$\gamma = 3.0$; (* Cooperativity coefficient *)
$\phi = 2.0$; (* Hill coefficient for the PMCA *)
$\beta = 0.4$; (* Stoichiometry coefficient *)
$\rho = 0.4$; (* Fraction of extruded Ca^{2+} available to interact with the CaR *)
$v_1 = \frac{3.854}{\text{caConc}(1+e^{6-0.003\text{caConc}})}\text{tempScalar}$; (* Velocity of Ca^{2+} supply with logisitic-equation form to simulate critical Ca^{2+} concentration *)
$k_1 = 3740.8 \times \text{tempScalar}$,
$k_{-1} = 115.22 \times \text{tempScalar}$,
$k_2 = 53.54 \times \text{tempScalar}$,
$k_3 = 1007.4 \times \text{tempScalar}$,
$k_{-3} = 18.1 \times \text{tempScalar}$,
$k_4 = 58.35 \times \text{tempScalar}$,
$k_{-4} = 633.01 \times \text{tempScalar}$,
$k_5 = 500 \times \text{tempScalar}$,
$K_{PMCA} = 0.425$;
$V_{PMCA} = 28 \times \text{tempScalar}$;

$K_{SERCA} = 0.18$;
ca[t] = caConc,
$v_2 = 53.54 \times$ tempScalar; (* Velocity of IP_3 degradation *)
sol = NDSolve[{
ca[t] = caConc,
$s_1'[t] = v_1 \text{ca}[t] - \frac{V_c}{V_e} k_1 s_1[t] x_1[t] + \frac{V_c}{V_e} k_{-1} x_2[t] + \frac{V_c}{V_e} \rho \frac{V_{PMCA} s_4[t]^{\phi}}{K_{PMCA}^{\phi} + s_4[t]^{\phi}}$, (* s_1 is extracellular [Ca^{2+}] sub-pool *)
$s_2'[t] = k_2 x[t] - k_3 s_2[t]^{\gamma} e_1[t] + \gamma k_{-3} x_1[t] - v_2 s_2[t] + k_{-4} x_3[t] - \frac{V_{ER}}{V_c} k_4 s_2[t] e_2[t]$, (* s_2 is [IP_3] *)
$s_3'[t] = \frac{V_c}{V_{ER}} \frac{V_{SERCA} s_4[t]}{K_{SERCA} + s_4[t]} \frac{1}{s_3[t]} - \beta k_5 s_3[t]^{\beta} x_3[t]$, (* s_3 is ER [Ca^{2+}] *)
$s_4'[t] = -\frac{V_c}{V_{ER}} \frac{V_{SERCA} s_4[t]}{K_{SERCA} + s_4[t]} \frac{1}{s_3[t]} - \frac{V_{PMCA} s_4[t]^{\phi}}{K_{PMCA}^{\phi} + s_4[t]^{\phi}} + \frac{V_{ER}}{V_c} \beta k_5 s_3[t]^{\beta} x_3[t]$, (* s_4 is cytosolic [Ca^{2+}] *)
$x_1'[t] = -\frac{V_e}{V_c} k_1 s_1[t] x_1[t] + (k_{-1} + k_2) x_2[t] + k_3 e_1[t] s_2[t]^{\gamma} - k_{-3} x_1[t]$, (* x_1 is $[E_1 S_2^{\gamma}]$ *)
$x_2'[t] = \frac{V_e}{V_c} k_1 s_1[t] x_1[t] - (k_{-1} + k_2) x_2[t]$, (* x_2 is $[S_1 E_1 S_2^{\gamma}]$ *)
$x_3'[t] = -\frac{V_c}{V_{ER}} k_{-4} x_3[t] + \frac{V_c}{V_{ER}} k_4 s_2[t] e_2[t]$, (* x_3 is $[E_2 S_2]$ *)
$e_1'[t] = -k_3 e_1[t] s_2[t]^{\gamma} + k_{-3} x_1[t]$, (* e_1 is [CaR] *)
$e_2'[t] = k_{-4} x_3[t] - \frac{V_c}{V_{ER}} k_4 s_2[t] e_2[t]$, (* e_2 is [IP_3R] *)
$s_1[0] = 0.5$, $s_2[0] = 0.44$, $s_3[0] = 500$, $s_4[0] = 0.0$, $x_1[0] = 0.0$, $x_2[0] = 0.0$,
$x_3[0] = 0.0$, ca[0] = caConc, $e_1[0] = 0.16$, $e_2[0] = 0.2$,
{s_1, s_2, s_3, s_4, x_1, x_2, x_3, e_1, e_2, ca},
{t, 0, 400}, MaxSteps → 20,000, MaxStepSize → 0.01, MaxStepFraction → 0.01, StartingStepSize → 0.1]; (* "sol" contains the solution to the kinetic equations with the given starting conditions for t = 0–100 s. *)
Plot[$s_4[t]$/.sol,{t, 0, 400},PlotRange → {{0, 400},{0, 0.4}}, PlotPoints → 2,000] (* Plot the intracellular [Ca^{2+}], S_4 *)

Appendix 2

Program written in *Mathematica* for the wavelet analysis used in the present work:

data = Import[″data.dat″]; (* Import the data set as a list of values *)
Hw := If [$\omega > 0$, 1, 0]; (* Definition of the Heaviside step function *)
$\omega_0 = 6$; (* Nondimensional frequency of the wavelet *)
$\psi f[\omega_-, s_-] = \sqrt{\frac{2\pi s}{\delta t}} \pi^{-\frac{1}{4}} \text{Hw}\, e^{\frac{-(s\omega - \omega_0)^2}{2}}$; (* Definition of the Morlet wavelet as a function of ω, time and s, the scale *)
$\delta t = \frac{1}{1.087454}$; (* Difference in time between successive data points. For our Fura-2 experiments, this was slightly over 1 s *)
$s_0 = 2\delta t$; (* Value of the first wavelet scale *)
$\delta j = 0.125$; (* Difference in power between successive wavelet scales *)
nN = Length[data]; (* Number of data points in the data set *)
fdata = Fourier[data]; (* Calculate the Fourier transform of the data set *)
$J = 60$; (* Number of scales to include in the wavelet transform *)
wt = Table[Table[0,{x, 0, nN}],{y, 1, J};] (* Initialization of the table receiving the wavelet transform result *)
For[$j = 0, j < J, j$++], {*pdata* =

$$\text{Table}\left[\psi f\left[\omega, 2\delta t \times 2^{j\delta j}\right], \left\{\omega, 0, \frac{2\pi}{\delta t}, \frac{\left(\frac{2\pi}{\delta t}\right)}{\text{nN} - 1}\right\}\right] //N;$$

$wt[[j+1]] = \frac{(\text{Abs}[\text{InverseFourier}[\text{fdata} \times \text{pdata}]])^2}{\text{Variance}[\text{pdata}]}$; (* Calculation and insertion of wavelet transform result *)
sca = Round$\left[\sqrt{2}\left(\text{Table}\left[2\delta t \times 2^{j\delta j}, \{j, 0, J\}\right]\right) \times \frac{1}{\delta t}\right]$;
(* Table of wavelet scales *)
coi = Table[Table[0,{x, 1, nN}],{y, 0, $J - 1$}];
Table[coi[[q, Table[x, {x, 1, sca[[q]]}]]] = Table[1,{x, 1, sca[[q]]}], {q, 1, J}; (* Initialization of the table receiving the cone of influence result *)
Table[coi[[q,Table[x,{x, Length[coi[[q]]] − *sca*[[q]] + 1, Length[coi[[q]]]}]]] = Table[1,{x, 1, sca[[q]]}], {q, 1, J}]; (* Calculation of cone of influence *)
coi = Mod[coi + 1,2]; (* Inversion of cone of influence *)
wtcoi = wt coi; (* Wavelet transform multiplied by cone of influence *)

References

Albrecht MA, Colegrove SL, Friel DD (2002) Differential regulation of ER Ca^{2+} uptake and release rates accounts for multiple modes of Ca^{2+}-induced Ca^{2+} release. J Gen Physiol 119:211–233. doi:10.1085/jgp.119.3.211

Bai M, Quinn S, Trivedi S, Kifor O, Pearce SH, Pollak MR, Krapcho K, Hebert SC, Brown EM (1996) Expression and characterization of inactivating mutations in the human Ca^{2+}-sensing receptor. J Biol Chem 271:19537–19545

Baker HL, Errington RJ, Davies SC, Campbell AK (2002) A mathematical model predicts that calreticulin interacts with the endoplasmic reticulum Ca^{2+}-ATPase. Biophys J 82:582–590. doi:10.1016/S0006-3495(02)75423-4

Benga G, Pop VI, Popescu O, Hodarnau A, Borza V, Presecan E (1987) Effects of temperature on water diffusion in human erythrocytes and ghosts–nuclear magnetic resonance studies. Biochim Biophys Acta 905:339–348. doi:10.1016/0005-2736(87)90462-7

Bracewell R (1999) The Fourier transform and its applications, 3rd edn. McGraw-Hill, New York

Bradbury RA, McCall MN, Brown MJ, Conigrave AD (1996) Functional heterogeneity of human term cytotrophoblasts revealed by differential sensitivity to extracellular Ca^{2+} and nucleotides. J Endocrinol 149:135–144. doi:10.1677/joe.0.1490135

Breitwieser GE (2006) Calcium sensing receptors and calcium oscillations: calcium as a first messenger. Curr Top Dev Biol 73:85–114. doi:10.1016/S0070-2153(05)73003-9

Breitwieser GE, Gama L (2001) Calcium-sensing receptor activation induces intracellular calcium oscillations. Am J Physiol Cell Physiol 280:C1412–C1421

Butz T (2006) Fourier transform for pedestrains. Springer, Berlin, p 201

Conigrave AD, Mun HC, Delbridge L, Quinn SJ, Wilkinson M, Brown EM (2004) L-amino acids regulate parathyroid hormone secretion. J Biol Chem 279:38151–38159. doi:10.1074/jbc.M406373200

Falcke M (2004) Reading the patterns in living cells—the physics of Ca^{2+} signaling. Adv Phys 53:255–440. doi:10.1080/00018730410001703159

Fioretti B, Franciolini F, Catacuzzeno L (2005) A model of intracellular Ca^{2+} oscillations based on the activity of the intermediate-conductance Ca^{2+}-activated K^+ channels. Biophys Chem 113:17–23. doi:10.1016/j.bpc.2004.07.037

Gosak M, Marhl M, Perc M (2008) Chaos out of internal noise in the collective dynamics of diffusively coupled cells. Eur Phys J B 62:171–177. doi:10.1140/epjb/e2008-00132-y

Goupillaud, P, Grossman AMJ, Morlet J (1984) Cycle-octave and related transforms in seismic signal analysis. Geoexploration 23:85–102. doi:10.1016/0016-7142(84)90025-5

Grynkiewicz G, Poenie M, Tsien RY (1985) A new generation of Ca^{2+} indicators with greatly improved fluorescence properties. J Biol Chem 260:3440–3450

Heinrich R, Schuster S (1996) The regulation of cellular systems. Chapman & Hall, New York

Hofer T (1999) Model of intercellular calcium oscillations in hepatocytes: synchronization of heterogeneous cells. Biophys J 77:1244–1256. doi:10.1016/S0006-3495(99)76976-6

Kaiser G (1994) A friendly guide to wavelets. Birkhäuser, Basel

Kamp TJ, Hell JW (2000) Regulation of cardiac L-type calcium channels by protein kinase A and protein kinase C. Circ Res 87:1095–1102

Kusters JM, Cortes JM, van Meerwijk WP, Ypey DL, Theuvenet AP, Gielen CC (2007) Hysteresis and bistability in a realistic cell model for calcium oscillations and action potential firing. Phys Rev Lett 98:098107. doi:10.1103/PhysRevLett.98.098107-1-4

Marhl M, Gosak M, Perc M, Jane Dixon C, Green AK (2008) Spatio-temporal modelling explains the effect of reduced plasma membrane Ca^{2+} efflux on intracellular Ca^{2+} oscillations in hepatocytes. J Theor Biol 252:419–426. doi:10.1016/j.jtbi.2007.11.006

Mulquiney PJ, Kuchel PW (2003) Modelling metabolism with *Mathematica*. CRC Press, Boca Raton

Mun HC, Franks AH, Culverston EL, Krapcho K, Nemeth EF, Conigrave AD (2004) The venus fly trap domain of the extracellular Ca^{2+}-sensing receptor is required for L-amino acid sensing. J Biol Chem 279:51739–51744. doi:10.1074/jbc.M406164/200

Perc M, Gosak M, Marhl M (2006) From stochasticity to determinism in the collective dynamics of diffusively coupled cells. Chem Phys Lett 421:106–110. doi:10.1016/j.cplett.2006.01.065

Perc M, Green AK, Dixon CJ, Marhl M (2008) Establishing the stochastic nature of intracellular calcium oscillations from experimental data. Biophys Chem 132:33–38. doi:10.1016/j.bpc.2007.10.002

Skupin A, Falcke M (2007) Statistical properties and information content of calcium oscillations. Genome Inf 18:44–53. doi:10.1142/9781860949920_0005

Sneyd J, Tsaneva-Atanasova K, Bruce JI, Straub SV, Giovannucci DR, Yule DI (2003) A model of calcium waves in pancreatic and parotid acinar cells. Biophys J 85:1392–1405. doi:10.1016/S0006-3495(03)74572-X

Tan YM, Cardinal J, Franks AH, Mun HC, Lewis N, Harris LB, Prins JB, Conigrave AD (2003) Autosomal dominant hypocalcemia: a novel activating mutation (E604K) in the cysteine-rich domain of the calcium-sensing receptor. J Clin Endocrinol Metab 88:605–610. doi:10.1210/jc.2002-020081

Torrence C, Compo GP (1998) A practical guide to wavelet analysis. Bull Am Meteorol Soc 79:61–78. doi:10.1175/1520-0477(1998)079<0061:APGTWA>2.0.CO;2

Wolfram S (2007) The *Mathematica* book. Wolfram Research Inc, Champaign

Young SH, Rozengurt E (2002) Amino acids and Ca^{2+} stimulate different patterns of Ca^{2+} oscillations through the Ca^{2+}-sensing receptor. Am J Physiol Cell Physiol 282:C1414–C1422

Young SH, Wu SV, Rozengurt E (2002) Ca^{2+}-stimulated Ca^{2+} oscillations produced by the Ca^{2+}-sensing receptor require negative feedback by protein kinase C. J Biol Chem 277:46871–46876. doi:10.1074/jbc.M207083200